43^{rd} European Rotorcraft Forum
Milan (*ITALY*), 12-15 September 2017
Paper 521

COMPUTATIONAL AEROACOUSTIC ANALYSIS OF PROPELLER INSTALLATION EFFECTS

Giulia Chirico – *g.chirico.1@research.gla.ac.uk*[a],
George N. Barakos – *George.Barakos@glasgow.ac.uk*[a,*] and
Nicholas Bown – *Nicholas.Bown@dowty.com*[b]

[a]CFD Laboratory, School of Engineering, University of Glasgow, G12 8QQ, UK
[b]Dowty Propellers, Anson Business Park, Cheltenham Road East, Gloucester, GL2 9QN, UK
[*]Corresponding author

ABSTRACT

In line with the goal of cleaner and quieter aircraft, this paper investigates propeller acoustics aiming to improve turboprops noise emissions, as they represent the best choice for short and medium range flights in terms of fuel efficiency. CFD is used to analyse the propeller-airframe interaction physics, and assess propeller installation effects, for a full scale twin-engined aircraft. The employed propellers represent advanced designs currently used in modern aircraft and the cases of co-rotating and counter-rotating top-in layout are considered. The URANS approach is used on grids of up to 195 M points aiming to directly extract from CFD the noise tonal content. Numerical results are first validated against model-scaled experimental data. A comparison between results of the full aircraft and a propeller in isolation is also carried out. Full aircraft predictions show significant differences in the external acoustics between port and starboard sides for the co-rotating case, with a louder noise generated by the inboard-up propeller. The counter-rotating layout shows a more regular distribution of overall noise, with on average slightly higher noise levels towards the front and the rear of the cabin. Acoustic predictions from an isolated propeller in axial flight significantly underestimate noise levels even on the fuselage sides where the aircraft masks the other propeller, showing the relevance of the propeller-airframe interactions in the evaluation of actual sound pressure levels in flight.

Keywords: *propeller acoustics, installation effects analysis, CFD*.

Copyright Statement© The authors confirm that they, and/or their company or organization, hold copyright on all of the original material included in this paper. The authors also confirm that they have obtained permission, from the copyright holder of any third party material included in this paper, to publish it as part of their paper. The authors confirm that they give permission, or have obtained permission from the copyright holder of this paper, for the publication and distribution of this paper as part of the ERF proceedings or as individual offprints from the proceedings and for inclusion in a freely accessible web-based repository.

Acronyms

ASPL	A-weighted Sound Pressure Level
BPF	Blade Passing Frequency
CFD	Computation Fluid Dynamics
OASPL	Overall A-weighted Sound Pressure Level
OSPL	Overall Sound Pressure Level
PSD	Power Spectral Density
RPM	Rounds Per Minute
SPL	Sound Pressure Level
TF	Transfer Function

Greek

Fuselage azimuthal coordinate [deg]	Θ
Reference blade azimuthal position [deg]	ψ_b

Latin

Acoustic Pressure field [Pa]	$p'(\mathbf{x}, t)$
Blade Root chord [m]	c
Free-stream density [kg/m^3]	ρ_∞
Free-stream Mach number [-]	$M_\infty = \frac{V_\infty}{a_\infty}$
Free-stream speed of sound [m/s]	a_∞
Free-stream velocity [m/s]	V_∞
Frequency [Hz]	f
Pressure coefficient [-]	$C_p = \frac{p}{\frac{1}{2}\rho_\infty V_\infty^2}$
Pressure field [Pa]	$p(\mathbf{x}, t)$
Propeller angular velocity [rounds/s]	$n = \frac{\mathrm{RPM}}{60}$
Propeller number of blades [-]	N_b
Propeller Radius [m]	R
Spacial coordinates [m]	x, y, z
Tip Mach number [-]	$M_{TIP} = \frac{V_{TIP}}{a_\infty}$
Tip Reynolds number [-]	$Re_{TIP} = \frac{V_{TIP} \cdot c \cdot \rho_\infty}{\mu}$
Vector position	$\mathbf{x}$
Viscosity [Pa·s]	μ
Wing chord [m]	c_w
Wing spacial coordinates [m]	x_w, y_w, z_w

Subscript

Root Mean Square of $(\cdot)$	$(\cdot)_{rms}$

Superscript

Time average of $(\cdot)$	$\overline{(\cdot)}$

1 INTRODUCTION

1.1 Motivation and Objectives

The aviation industry aims to develop aircraft with low environmental impact, as regards reduction in fuel burnt, as well as acoustic emissions. In the European market, where up to 95% of the routes is constituted by short and medium range flights, propeller-driven aircraft represent the best choice, because of their considerably higher fuel efficiency in comparison with an equivalent turbofan powered aircraft. However, the noise emitted by current turboprops is still higher that future noise certification may require. The European Commission has, in fact, set as targets a cut of the perceived acoustic footprint of flying aircraft by 50% for 2020[1], and a total noise abatement of 65% for 2050[2], relative to the capabilities of typical new aircraft in 2000. In addition, because of the discrete, few, tone components forming the propeller sound spectra, turboprop noise is perceived by passengers as more annoying than turbofan noise. Hence, the challenge is to look for ways to improve the acoustics of propellers without a high performance penalty.

Going in this direction, in 2012, Dowty Propellers promoted the IMPACTA project[3] to investigate propeller noise, aiming for a reduction and/or a modification in the acoustic spectra generated by the whole propulsion system of a turboprop aircraft. In collaboration with Aircraft Research Association (ARA), the Netherlands Aerospace Centre (NLR) and the University of Glasgow, experimental and numerical work was carried out during the project to evaluate aerodynamics and acoustics of innovative propeller designs in both isolated and installed configurations. Starting from the IMPACTA project, this research uses Computational Fluid Dynamic (CFD) to investigate the physics of propeller-airframe interaction, and to quantify propeller installation effects on acoustics. Having this objective, a complete twin-engined turboprop aircraft is studied, and results are compared against an isolated propeller case. In particular, the exterior acoustic field on the fuselage is analysed. Both configurations of co-rotating and counter-rotating propellers are considered, the first one being the case of the majority of civil turboprops and the second found in some military designs.

1.2 Past Work

Pushed by the high oil prices at the turn of the eighties and nineties, the aviation industry re-started research on propellers, because of their high efficiency. The importance of a low noise radiation propulsion system was also already understood at that time, being linked to the aircraft costs. Major efforts were therefore undertaken to study propeller aerodynamics and acoustics, when installed on the aircraft, via experiments and numerical calculations.
The PTA (*Propfan Test Assessment*) program of NASA deeply investigated the noise characteristics of an advanced propeller, the SR-7L[4, 5], under actual flights conditions via a full-scale in-flight campaign[6, 7] covering a wide set of operating conditions. The large dataset obtained was used to assess the accuracy of noise prediction methods: good agreement was found regarding trends and absolute levels in [8, 9] considering both aerodynamics and aeroelasticity as input to the propeller noise code[10, 11] and including fuselage scattering and refraction [12]; direct near-field noise estimates of 3D unsteady Euler com-

putations were evaluated against two frequency-domain methods[13, 14] in [15] concluding that the direct noise computation, as it naturally accounts for these non-linear propagation effects, can be a "viable and reliable" near-field noise technique provided an appropriate grid resolution.

In Europe, the propeller slipstream-airframe interaction for a typical commuter flying at transonic speed was studied within a series of projects. GEMINI (*basic test rig for a GEneric Model for tunnel test on airframe propulsion INtegration with emphasIs on advanced propellers*) investigated the aerodynamics of the problem via wind tunnel experiments[16] and Euler/Navier-Stokes computations[17, 18]; SNAAP examined the acoustics of the isolated high-speed propeller. APIAN (*Advanced Propulsion Integration for Aerodynamics and Noise*) analysed aerodynamic and acoustic interference effects with wind tunnel tests[19] and Euler simulations combined with acoustic codes for radiation and scattering and rarefraction by ONERA and NLR [20].

The Aeronautical Research Institute of Sweden, FFA, carried out first an extensive low-speed aerodynamic experimental campaign on a propeller/nacelle/wing scaled model[21, 22], which was also simulated with a time-averaged panel code including a propeller slipstream model[23, 24] and unsteady Euler/Navier-Stokes computations with TAU[25]. Afterwards, in collaboration with SAAB, FFA performed in-flight acoustic measurements of exterior and interior sound field on the twin-engined co-rotating turboprop SAAB 2000[26], showing that the cabin noise is dominated by the fist three propeller tones and is louder on the fuselage starboard side where the propeller approaches when moving upwards.

2 COMPUTATIONAL METHODS AND SETUP

2.1 *The Flow Solver HMB3*

The parallel CFD solver HMB3 (Helicopter Multi Block)[27, 28] of the University of Glasgow was employed to perform all numerical simulations of this work. HMB3 solves the 3D Navier-Stokes equations in dimensionless integral form using the Arbitrary Lagrangian Eulerian (ALE) formulation for time-dependent domains with moving boundaries:

$$\frac{d}{dt}\int_{V(t)} \mathbf{W} dV + \int_{\partial V(t)} (\mathbf{F}_i(\mathbf{W}) - \mathbf{F}_v(\mathbf{W})) \cdot \mathbf{n} dS = \mathbf{S} \quad (1)$$

where $V(t)$ is the time dependent control volume, $\partial V(t)$ its boundary, $\mathbf{W}$ the vector of the conservative variables $(\rho, \rho u, \rho v, \rho w, \rho E)^T$, $\mathbf{F_i}$ and $\mathbf{F_v}$ the inviscid and viscous fluxes respectively and $\mathbf{S}$ the source term. The viscous stress tensor is usually approximated using the Boussinesq hypothesis[29], but an explicit algebraic Reynolds stress model[30] is also available. Severals turbulence models, of both URANS and hybrid LES/URANS families, are implemented in the solver. In this work, the $k-\omega$ SST turbulence model[31] was used to close the URANS equations.

To reduce the computational effort, the case of an isolated propeller in axial flight conditions is formulated as steady flow problem of a single blade, assuming the flow periodic in both space and time. In this case, therefore, a non-inertial frame of reference is adopted and the ALE formulation (1) is modified to account for the centripetal and Coriolis acceleration terms appearing via a mesh velocity and a momentum source term[28].

The Navier-Stokes equations are discretized using a cell-centered finite volume approach on a curvilinear coordinate system, since body-conforming grids are adopted. The system of equations that has to be solved is thus:

$$\frac{d}{dt}\left(\mathbf{W}_{i,j,k}\mathcal{V}_{i,j,k}\right) + \mathbf{R}_{i,j,k} = 0 \quad (2)$$

where $\mathbf{W}_{i,j,k}$ is the vector of conserved variables of each cell, $\mathcal{V}_{i,j,k}$ denotes the cell volume and $\mathbf{R}_{i,j,k}$ represents the flux residual.

Osher's upwind scheme[32] is used for the convective fluxes because of its robustness, accuracy and stability properties. The MUSCL variable extrapolation method[33] is employed to provide second-order accuracy and spurious oscillations across shock waves are removed with the use of the van Albada limiter [34]. To achieve fast convergence, the integration in time is performed with an implicit dual-time method. The linear system is solved using the generalised conjugate gradient method with a BILU[35] factorisation as a pre-conditioner.

Boundary conditions are set by using ghost cells on the exterior of the computational domain.

To obtain an efficient parallel method based on domain decomposition, different methods are applied to the flow solver[36] and the Message Passing Interface MPI tool is used for the communication between the processors.

2.2 *CFD Solver Validation*

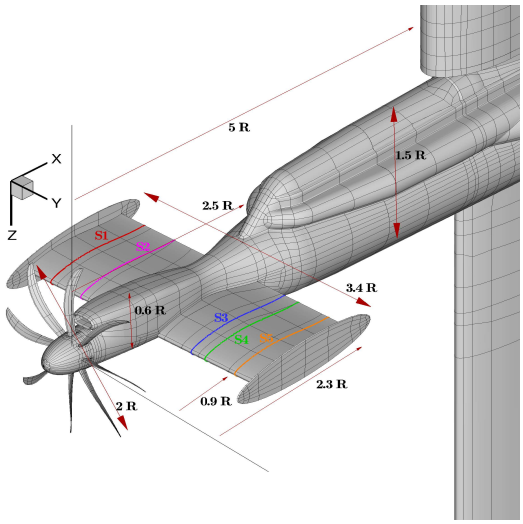
The in-house CFD solver HMB3[27, 28] was first validated for propeller flows, in both isolated and installed propeller configurations, by comparison with experiments.

HMB3 numerical predictions of the pressure coefficient distribution on the propeller blades were evaluated using the measurements of the unswept JORP propeller[37]. Results were presented in [38]. Some discrepancies in the suction peak values can be observed for some radial stations, probably due to a different blade pitch angle; nevertheless, the normal force trend is well captured and an overall good agreement is seen.

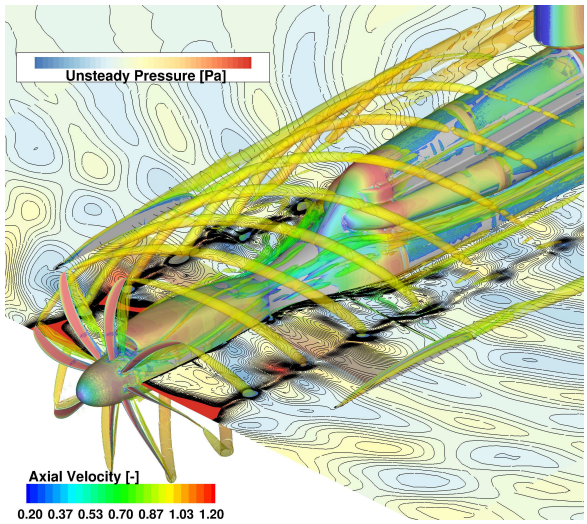
The IMPACTA experimental dataset[39] was employed to assess the accuracy of the HMB3 results regarding the propeller slipstream predictions. The IMPACTA wind tunnel model is a scaled, installed turboprop power-plant that consists of propeller, nacelle with intake, and a stub wing with

Number of blades N_b	8	Free-stream Mach number M_∞	0.5
Radius R	0.457 m	Free-stream incidence w.r.t. thrust line	-2 deg
Root chord c	0.044 m	Tip Mach number M_{TIP}	0.578
Angular velocity n	$\sim$ 4050 RPM	Tip Reynolds number Re_{TIP}	0.5e6

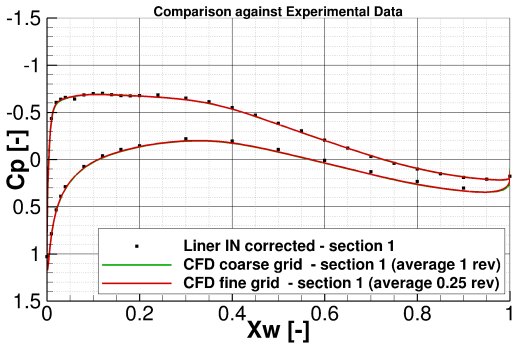
Table 1: HMB3 validation - IMPACTA wind tunnel model: propeller parameters and test conditions.



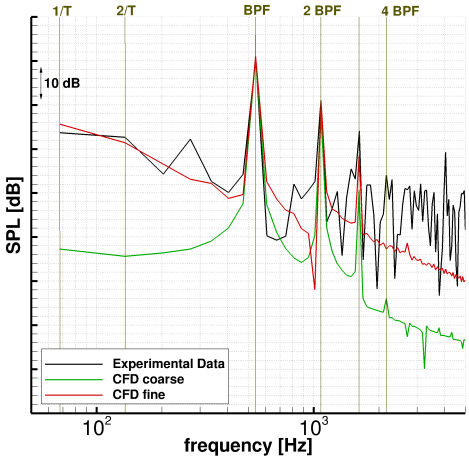
(a) Geometry of model (scale 1 to 4.83). Dimensions reported as function of the model scale propeller radius R. The propeller angular rotation is clockwise when viewed from the rear.



(b) HMB3 results using the fine mesh: wake (iso-surface of Q criterium, adimensional value equal to 0.005, coloured by adimensional axial velocity) and acoustic pressure field visualisation.



(c) Chord-wise pressure coefficient distribution on the wing: comparison between averaged CFD results of HMB3 and experiments by ARA. Span-wise section on the port wing, at 90% of the propeller radius.



(d) SPL spectra: comparison between numerical results of HMB3 and experimental data from Kulite measurements by ARA. Sensor on the port lower wing, at 92% of the propeller radius on the wing span and at 5% on the chord.

Figure 1: IMPACTA wind tunnel scaled model at cruise conditions.

steady and unsteady pressure sensors installed. Figure 1(a) shows geometry and dimensions of the model which was mounted inverted in the wind tunnel. Table 1 reports propeller parameters and tests conditions representative of a cruise case. A structured multi-block CFD grid was created using the sliding plane technique[40], to enable the relative motion of the propeller, and have a different topology and/or number of cells in different parts of the computational domain. Different mesh densities were considered, with a coarse grid of about 20.1 M cells and a finer grid with a spacial resolution doubled in all directions (i.e. $\sim$ 161.3 M cells). No simplifications of the model geome-

try were adopted in the mesh generation, while the wind tunnel walls were not represented in the CFD computation as the experimental data were corrected to account for the channel effects. URANS (Unsteady Reynolds Averaged Navier-Stokes equations) simulations were carried out with a temporal resolution equivalent to 1 degree of propeller azimuth, i.e. 360 steps were resolved per propeller revolution. A visualisation of the flow features is reported in Figure 1(b). Steady pressure taps on the model wing surface enable a comparison between numerical results of HMB3 and wind tunnel measurements (see, as example, Figure 1(c)). Numerical probes, located at the cell center closest to the experimental Kulite™ sensors position, allowed to record the pressure time history and evaluate the predicted noise spectra (see, as example, Figure 1(d)). Results are extensively presented in [41]. Globally, a good agreement is seen regarding both aerodynamics and acoustics, showing that HMB3 is able to accurately represent the aerodynamic interference propeller-airframe and to capture dominant noise tones of the acoustic near-field with adequate precision.

2.3 *Test Cases*

The IMPACTA Baseline propeller is employed in this research: it is an eight bladed new-generation propeller with extremely low activity factor, designed to operate at $M_\infty = 0.5$ and ~ 850 RPM, at high blade loading conditions. Geometric and operating parameters of the IMPACTA Baseline propeller are summarised in Table 2.
A typical large high-wing twin-engined turboprop commercial airplane is considered, similar to the Fokker 50. Computational geometry and dimensions are shown in Figure 3(b). URANS computations of the complete aircraft are carried out for both configurations of co-rotating and counter-rotating propellers. As co-rotating case, the conventional layout with propellers rotating clockwise, as seen from the cockpit, was selected; instead, the starboard propeller rotates counterclockwise in the case of counter-rotating propellers, i.e. a top-in configuration (see Figure 2). Details of the simulated conditions, representative of a cruise state, are reported in Table 2. Likewise the validation test cases, a temporal resolution corresponding to 1 degree of propeller azimuth was chosen. Numerical probes are included in the unsteady simulations to directly record the pressure signal on the fuselage in the main propeller region of influence, on the wings and at the engine intakes.
The study of the acoustic field of the propeller in isolation is performed using the RANS equations for a single blade and axial flight conditions. The noise can then be evaluated, at the point of interest $\mathbf{x}$, from the equivalent unsteady acoustic pressure signal $p'(\mathbf{x},t) \doteq p(\mathbf{x},t) - \overline{p(\mathbf{x},t)}$ which is reconstructed *a posteriori* from the steady CFD solution. In particular, the acoustic analysis was performed on an array of 32 by 33 points arranged on a half-cylinder miming the starboard side of the high-wing aircraft fuselage. Figure 4(c) shows as example the instantaneous pressure distribution on the idealised fuselage when $\psi_b = 0deg$.
Sound Pressure Level (SPL) and Overall SPL (OSPL) are computed as follows:

$$\begin{cases} SPL(f) = 10\log_{10}\left(\frac{PSD(p')}{{p_{ref}}^2}\right) \text{ dB}, \\ OSPL = 10\log_{10}\left(\frac{{p'_{rms}}^2}{{p_{ref}}^2}\right) \text{ dB}, \end{cases} \tag{3}$$

where $p_{ref} = 2 \cdot 10^{-5}$ Pa, which corresponds to about the threshold of hearing for a sinusoidal signal at roughly 2kHz. Note that, since the main focus of the acoustic analysis in this work was on the propeller tonal noise, (U)RANS computations were selected as the cheapest CFD method; no attempt was made at this stage to study also the broadband noise content.

2.4 *Computational Grids*

The ANSYS-Hexa meshing software[42] was used to generate all computational grids for this work.
For the propeller installed configurations, a fully-matched body-fitted grid was built around the whole aircraft, employing an "O" grid topology surrounding the surfaces of fuselage, wings and nacelles. Refinement was applied in areas which had proved critical in preliminary tests, such as the fuselage-wing junction. The computational grid was prepared on half of the model and then mirrored, to ensure a perfectly symmetric mesh. Similarly, the propeller grids were generated from a one-blade grid, copy-rotating (and mirroring when necessary). The sliding plane technique[40] was employed between aircraft and propeller grids. The grids for co- and counter-rotating cases were thus obtained just changing the grid component for the starboard propeller during the assembling process. The chimera overset method[43] is used to immerse the aircraft mesh in a Cartesian background grid, so that the computational domain is extended until the far-field where free-stream boundary conditions are applied. The grid layout is shown in Figure 3, with the multi-block topology and mesh. Globally, the full aircraft grid counts about 170 M cells, of which $\sim$132 M belong to the aircraft body and $\sim$16.5 M to each propeller.
Regarding the propeller in isolation, since axial flight conditions were assumed, the grid represents $1/N_b$ of the computational domain, including a single propeller blade mounted on the spinner. A classic "C−H" topology was adopted for the blocks around the blade. The computational domain, with relative dimensions, and grid topology are shown in Figure 4. The grid is matched on the symmetry planes where periodicity boundary conditions are applied. This implies that some areas of the grid have slightly stretched cells due to the high pitch and sweep of the blade. The total grid size is of 11.25 M cells.

Number of blades N_b	8	Free-stream Mach number M_∞	0.5
Radius R	2.21 m	Free-stream incidence w.r.t. thrust line	-2 deg
Root chord c	0.213 m	Helical Mach number at 0.95R	0.789
Blade pitch angle at 0.7R	$\sim 51°$	Tip Reynolds number Re_{TIP}	1.24e06
Angular velocity n	$\sim$ 850 RPM	Altitude	7620 m
Required Thrust	7852 N	Temperature	248.62° C

Table 2: IMPACTA Baseline propeller parameters and cruise operating conditions.



(a) Co-rotating propellers. (b) Counter-rotating propellers.

Figure 2: Propeller rotational direction definition.

3 ANALYSIS OF THE RESULTS

3.1 Comparison between Co-Rotating and Counter-Rotating Layouts

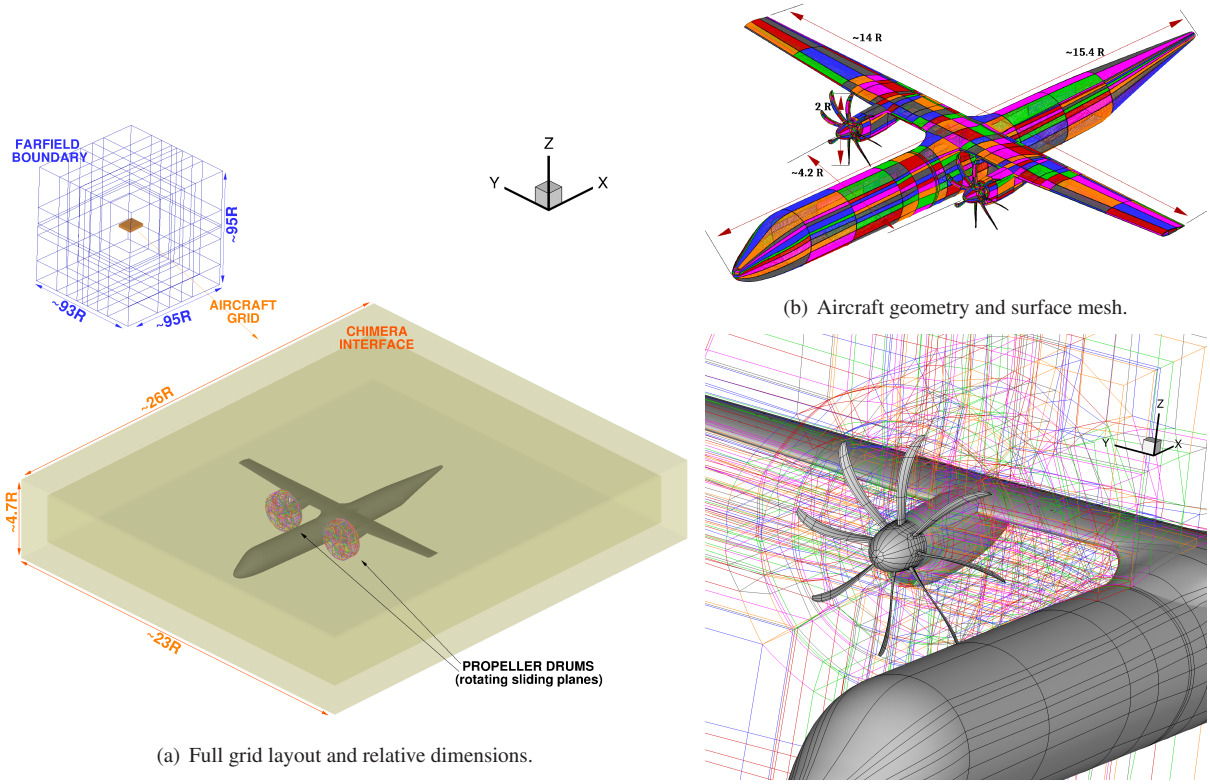
The effect of the rotational direction is now discussed aiming to find the best configuration to install the propellers on the aircraft from the acoustic prospective.

The pressure distribution on the aircraft and the flow vortices is presented in Figure 5. As expected, we can observe a perfect symmetry of the flow features and pressure distribution for the counter-rotating case, while differences between port and starboard side are visible in the co-rotating case. From the wing point of view, a depression area which extends from the nacelle location to the wing junction on the starboard side for the co-rotating configuration can be seen. No attempt to trim the aircraft was made for the co-rotating case, yielding to a thrust difference between port and starboard propeller of around 0.2%. As can be seen from the wake visualisations, the adopted mesh resolution preserves the propeller wake up to the aircraft tail. The interaction of the blade tip vortices with the wing is well captured by the CFD simulation. The vortices generated from the wing tips, the nacelles and the inclination of the aft fuselage are visible.

Figure 6 shows the OSPL distribution on the aircraft for both layouts. Areas of higher noise are visible on the fuselage around the propeller plane, nacelles and wing regions affected by the propeller slipstream. Footprints of the wake tip vortices clearly appear on the wings at the boundary of the slipstream. Also regarding the acoustics, the symmetry of the developed field in the case of counter-rotating case can be observed as expected. Globally, the counter-rotating layout shows a more regular and smooth noise pattern, though experiencing slightly higher noise levels, while an non-uniform behavior, with marked low-picks of OSPL, are seen in the co-rotating configuration, both at the front and at the rear part of the fuselage. Comparing the sound at the port and starboard fuselage sides for the co-rotating layout, it can be seen that the first displays lower noise levels. Therefore, the inboard-down propeller seems beneficial with respect to the inboard-up as concerns the acoustics. Finally, for the co-rotating case, a region of high OSPL is noted on the low starboard wing near the junction with the nacelle.

Visualisation of the acoustic pressure field on various planes is presented in Figures $7-9$. It can be seen that the current mesh resolution captures the noise generated by the blades tip and to preserve the acoustic waves further downstream, up until the aircraft tail, even if some attenuation is visible. Noise travelling in the up-stream direction is also noted. Variation in the direction of the sound waves propagated downstream the wing, with a downward tilt, are seen. The slipstream contraction is also visible. Noise emitted at the back of the nacelles is as well observed. Again, the acoustic field of the counter-rotating case is symmetric and the differences between port and starboard sides in the case of counter-rotating propellers are evident. The noise generated by the interaction of the blade tip acoustic waves with the inboard part of the starboard wing appears to be significantly louder in the co-rotating case, thus confirming the benefits of the inward-down propeller rotation. Finally, it seems that slightly lower noise levels are generated at the fuselage-wing junction.

Figure 10 shows the pressure signals from selected numerical probes located on the fuselage at the propeller plane. As expected, for the co-rotating configuration, differences in the signals recorded at the same position on the port and starboard side of the aircraft fuselage are clearly visible. In this case, towards the bottom of the fuselage the acoustic pressure signals of the correspondent probes become closer. In line with the OSPL results, it can be seen that at this fuselage station the starboard side experiences larger fluctuations, and louder noise, than the port side, apart from



(a) Full grid layout and relative dimensions.

(b) Aircraft geometry and surface mesh.

(c) Grid topology: propeller blocks detail.

Figure 3: High-wing twin-engined turboprop aircraft: computational grid. R is the propeller radius.

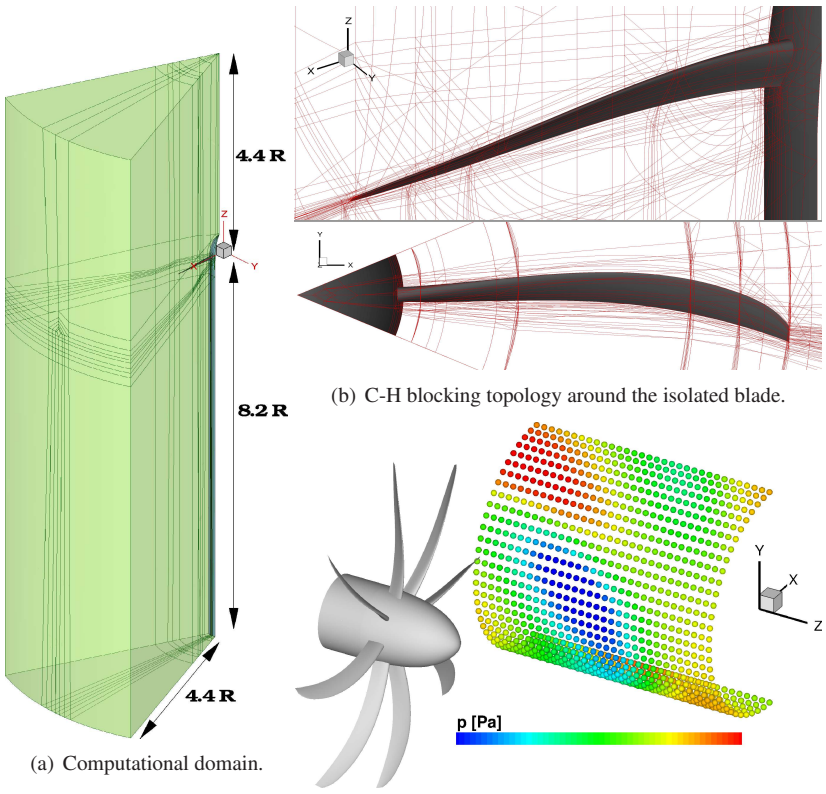
one position situated towards the top of the fuselage. Regarding the counter-rotating layout, a complete overlap of the acoustic pressure signals on the port and starboard sides is seen as expected from the symmetry of the propeller installation option. Finally, for both configurations, the presence of a second frequency in some of the signals can be noted.

3.2 Comparison against Propeller in Isolation

Installed and isolated acoustic results are now compared. The noise field on the fuselage starboard side for a top-out rotating propeller is considered, which was found to be the noisiest in the previous paragraph.

It has to be noted that the installed propeller, at the tested conditions, delivers a higher thrust than the propeller in isolation in axial flight. In particular, a difference of about 5.63% is registered.

Figure 11(a) shows the OSPL distribution on the fictitious fuselage reconstructed from the steady RANS solution of the isolated propeller in axial flight. The unsteady pressure time histories of three locations on the fuselage, located at the propeller plane, are presented in Figure 11(c) against the corresponding probe signals of the co-rotating full aircraft computation. The SPLs of the first two tones as a function of the fuselage azimuth angle are shown in Figure 11(b). As can be seen, the noise distribution estimated from the isolated computation is similar to the installed, at least in the vicinity of the propeller plane and in the region where interferences with the other propeller do not occur because of the fuselage blockage effect. However, the sound levels are significantly underestimated, as it is also evident from the large difference in the amplitude of the pressure fluctuations. An average discrepancy of about 9 dB for the SPL of the first tone is registered for the central part on the fuselage side. A small shift in phase in the unsteady pressure signals between isolated and installed cases is also visible. Finally, the difference between the SPL of first and second tone is about 2 dB smaller in the installed case than in the isolated, axial flight case. These differences are more likely to be due to the disturbed propeller inflow and the installation effects e.g. fuselage reflections and refractions, than to the propeller thrust difference. Applying the ESDU method[44] derived from Gutin's theory[45] the registered thrust difference would yield differences of +0.28 dB for the first, and -0.25 dB for the second tones. Future simulations under the same inflow conditions will investigate more deeply this aspect.



(a) Computational domain.

(b) C-H blocking topology around the isolated blade.

(c) $p(\mathbf{x}, t)|_{\psi_b=0deg}$ on the exterior of the idealised fuselage.

Figure 4: IMPACTA Baseline propeller in isolated configuration: computational setup.

4 CONCLUSIONS AND FUTURE WORK

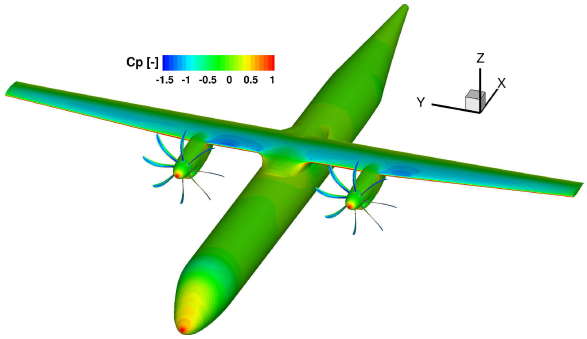
Near-field tonal noise of a twin-engined turboprop aircraft was studied using the CFD solver HMB3 previously validated against experimental data. A standard co-rotating civil configuration and a counter-rotating top-in layout were considered. The first shows a quite irregular OSPL distribution on the aircraft fuselage, although it seems globally slightly quieter than the counter-rotating layout. The louder noise on the fuselage is observed on the starboard side in the case of the co-rotating propellers, thus indicating the inboard-down propeller rotation beneficial from the acoustic point of view. Acoustic predictions from an isolated propeller in axial flight significantly underestimate noise levels even on the fuselage sides where the aircraft masks the effects of the other propeller, showing the relevance of the propeller-airframe interactions. The simulation of the full-aircraft seems therefore to be necessary not only to capture the details of the complex acoustic field that generates from the interactions between the two propellers and the airframe, but also to evaluate the actual noise levels in flight.

Future developments of this research address to investigate other propeller installation layouts to find the quieter option: *(i)*counter-rotating propellers in configuration top-out, which have proven to be more efficient from the aerodynamic point of view[46], will be considered, *(ii)*the effect of a constant propeller phase shift will be analysed, since experimental and analytical works [47, 48, 49, 50, 51] have shown that synchrophasing can reduce noise levels. The cabin interior noise will also be considered in the layouts assessment.
Furthermore, a different blade design, which had proven to be considerably quieter than the baseline when studied in isolation [41], will be tested on the aircraft to evaluate if the noise reduction is maintained once installed.
On another hand, future work seek to inquire into the employed CFD method: noise predictions with other techniques with lower turbulent viscosity than URANS, such as SAS[52] and DES[53, 54] will be analysed; the performance and the accuracy of the high-order scheme available in HMB3 [55] will be evaluated.

ACKNOWLEDGEMENTS

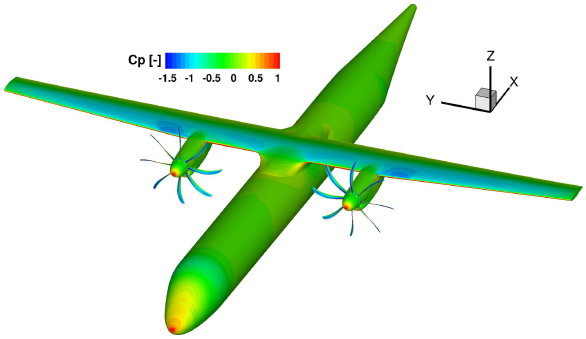
This research is supported by Dowty Propellers[56]. Results were obtained using the EPSRC funded ARCHIE-WeSt High Performance Computer (www.archie-west.ac.uk) and the EPCC's Cirrus HPC Service (https://www.epcc.ed.ac.uk/cirrus), that are gratefully acknowledged for the time allocated. The authors would also

CO-ROTATING LAYOUT

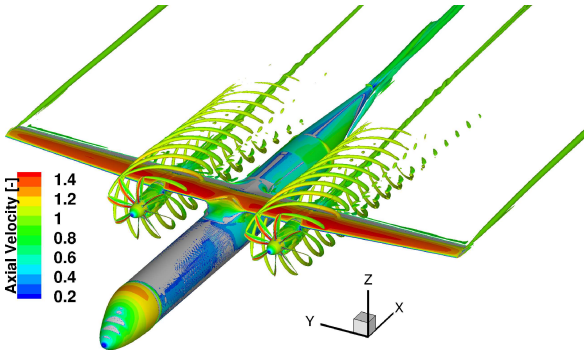


(a) Pressure distribution on the aircraft ($\psi_b = 270deg$).

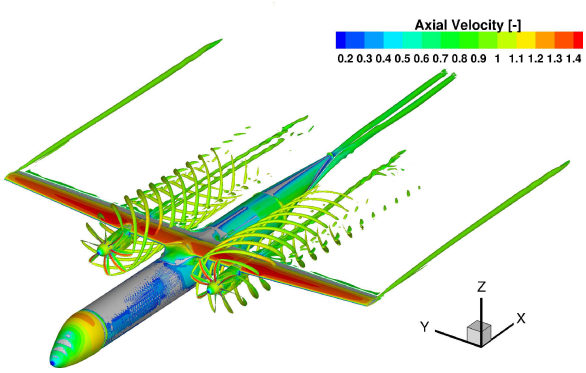
COUNTER-ROTATING TOP-IN LAYOUT



(b) Pressure distribution on the aircraft ($\psi_b = 90deg$).



(c) Wake structures: iso-surfaces of Q, colored by non dimensional axial velocity ($\psi_b = 270deg$).



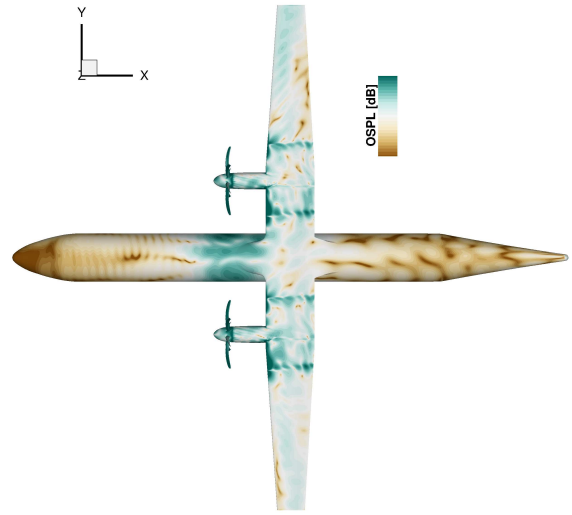
(d) Wake structures: iso-surfaces of Q, colored by non dimensional axial velocity ($\psi_b = 90deg$).

Figure 5: Visualisation of the instantaneous surface pressure and flow-field.

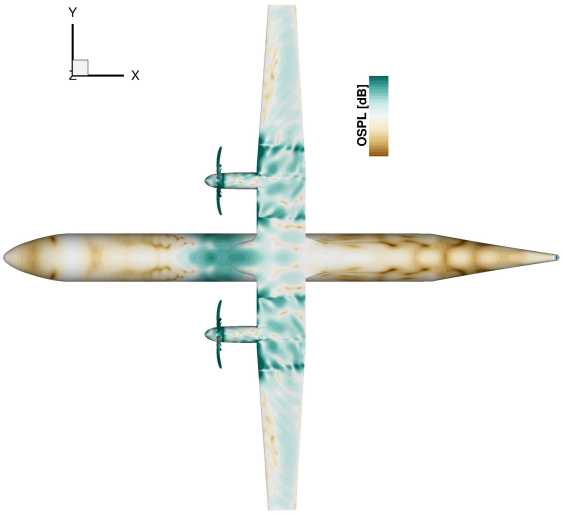
like to thank ARA and NLR for the use of the experimental data, and Ivan Malcevic of GE Global research for the supply of the wind tunnel model CAD geometry.

CO-ROTATING LAYOUT

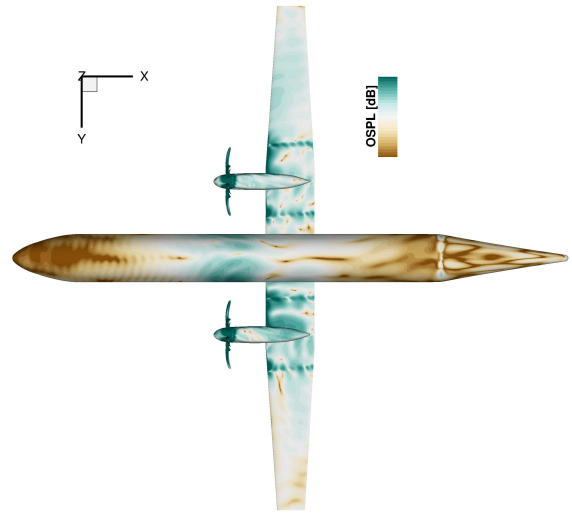
COUNTER-ROTATING TOP-IN LAYOUT



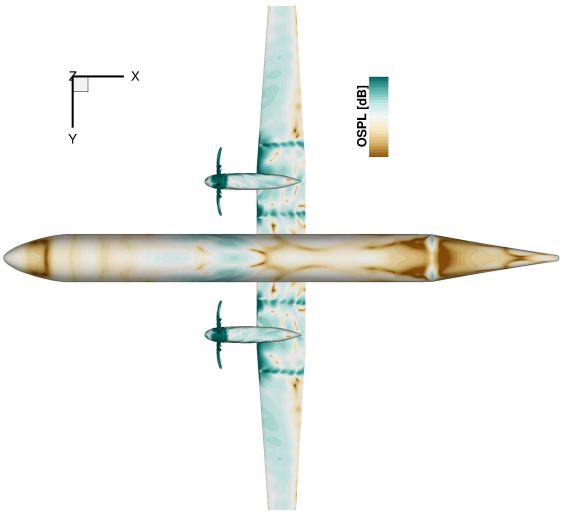
(a) Top view.



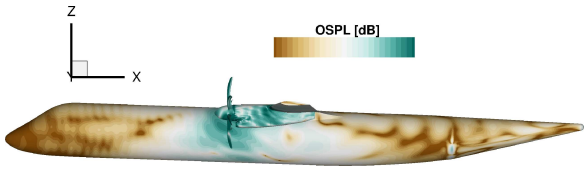
(b) Top view.



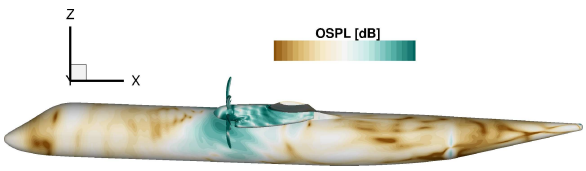
(c) Bottom view.



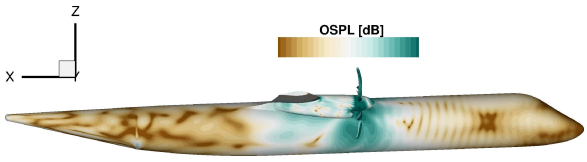
(d) Bottom view.



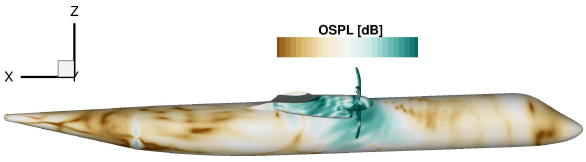
(e) Port side.



(f) Port side.



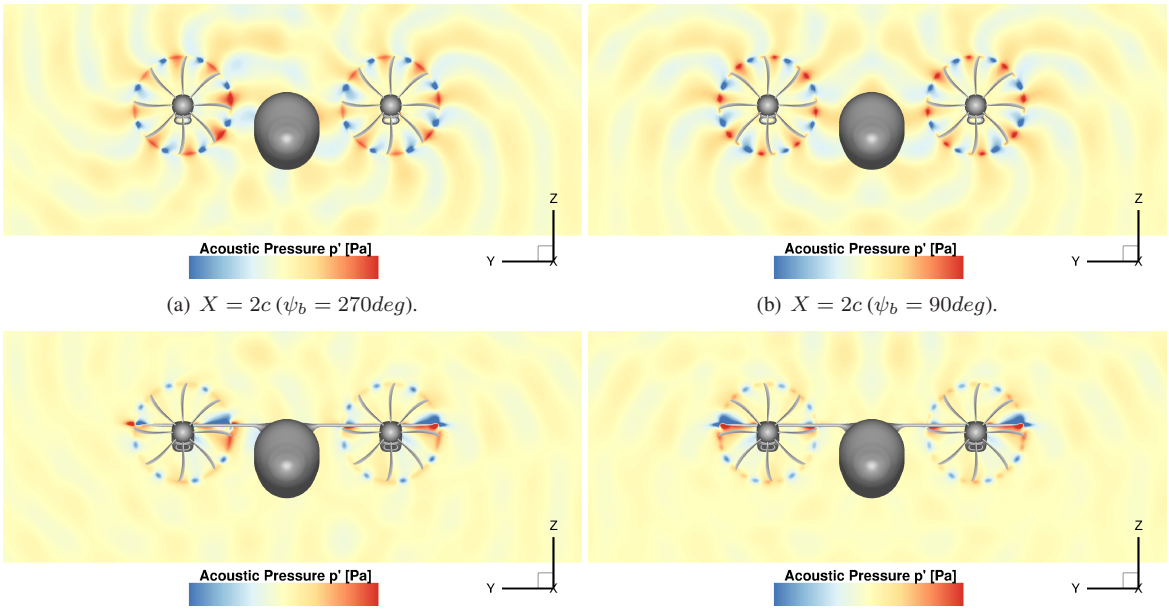
(g) Starboard side.



(h) Starboard side.

Figure 6: OSPL on the aircraft surface - URANS results from 45 deg. Colour range equal to 45 dB.

CO-ROTATING LAYOUT COUNTER-ROTATING TOP-IN LAYOUT

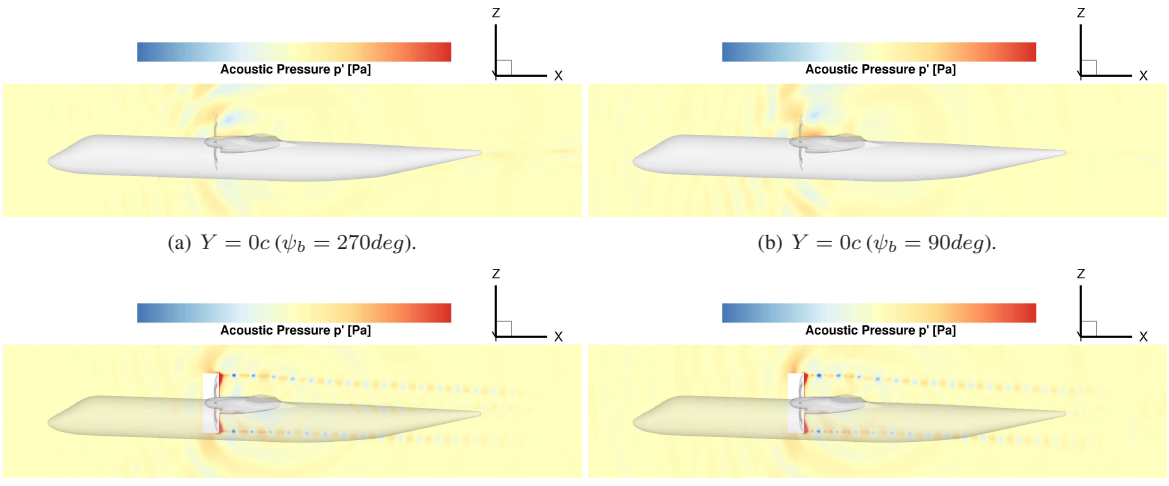


(a) $X = 2c$ ($\psi_b = 270deg$). (b) $X = 2c$ ($\psi_b = 90deg$).

(c) $X = 10c$ ($\psi_b = 270deg$). (d) $X = 10c$ ($\psi_b = 90deg$).

Figure 7: Instantaneous acoustic pressure field, visualised in transversal planes.

CO-ROTATING LAYOUT COUNTER-ROTATING TOP-IN LAYOUT

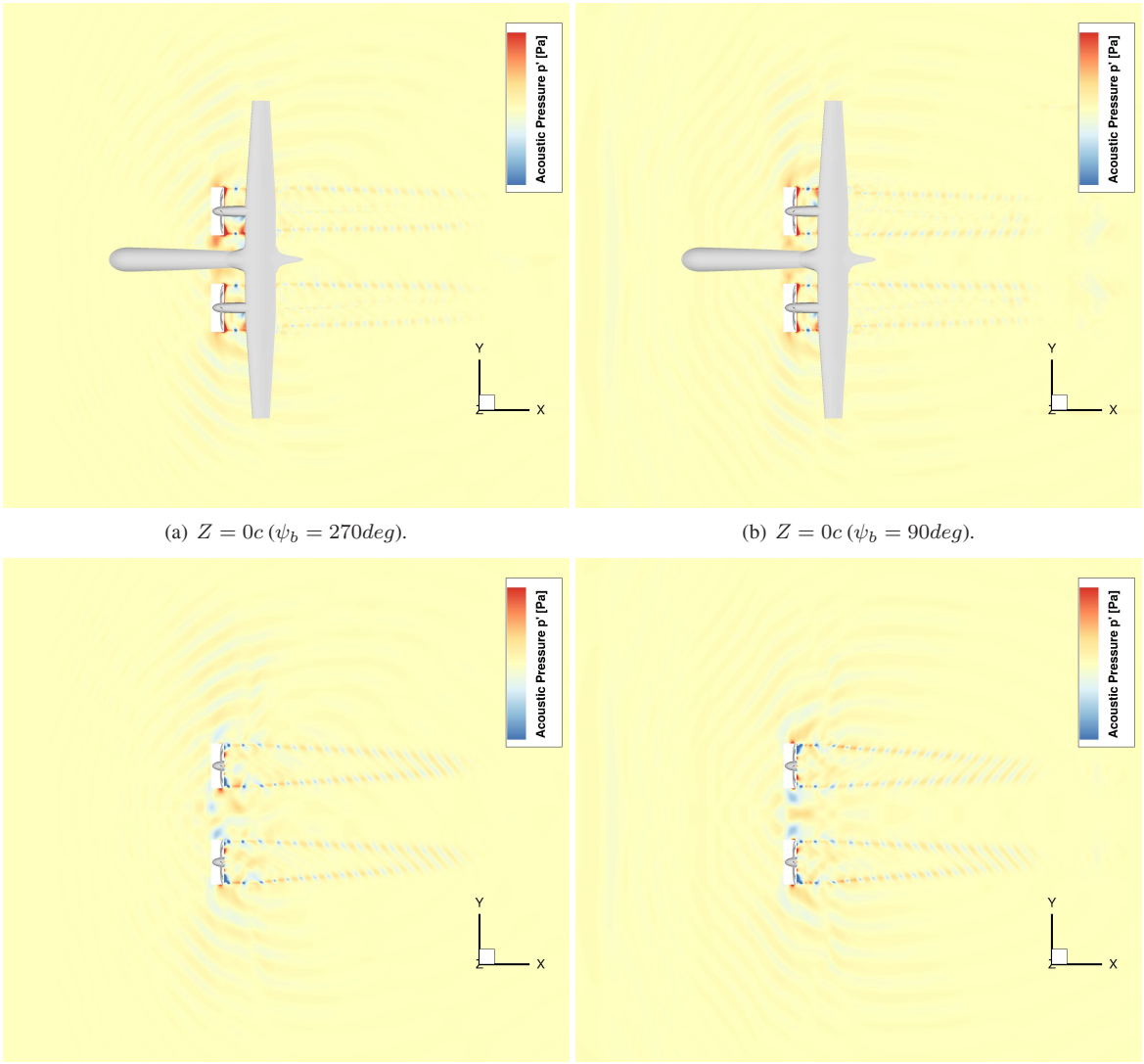


(a) $Y = 0c$ ($\psi_b = 270deg$). (b) $Y = 0c$ ($\psi_b = 90deg$).

(c) $Y = 22c$, i.e. starboard propeller plane ($\psi_b = 270deg$). (d) $Y = 22c$, i.e. starboard propeller plane ($\psi_b = 90deg$).

Figure 8: Instantaneous acoustic pressure field, visualised in lateral planes.

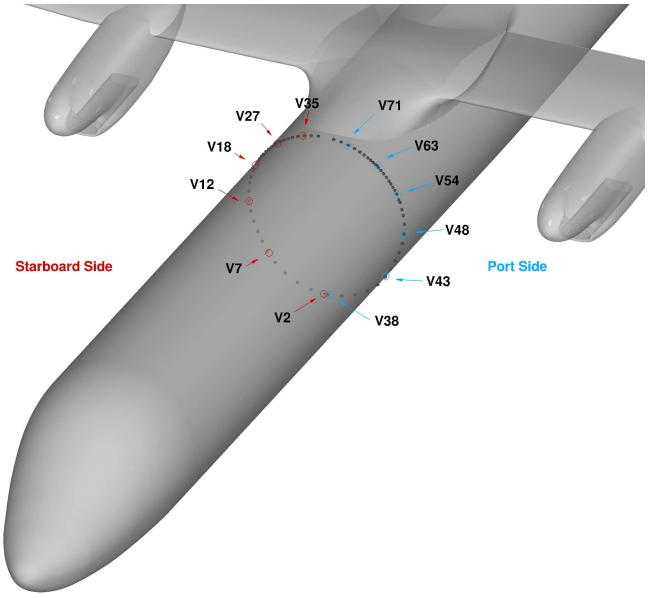
CO-ROTATING LAYOUT COUNTER-ROTATING TOP-IN LAYOUT



(a) $Z = 0c$ ($\psi_b = 270deg$). (b) $Z = 0c$ ($\psi_b = 90deg$).

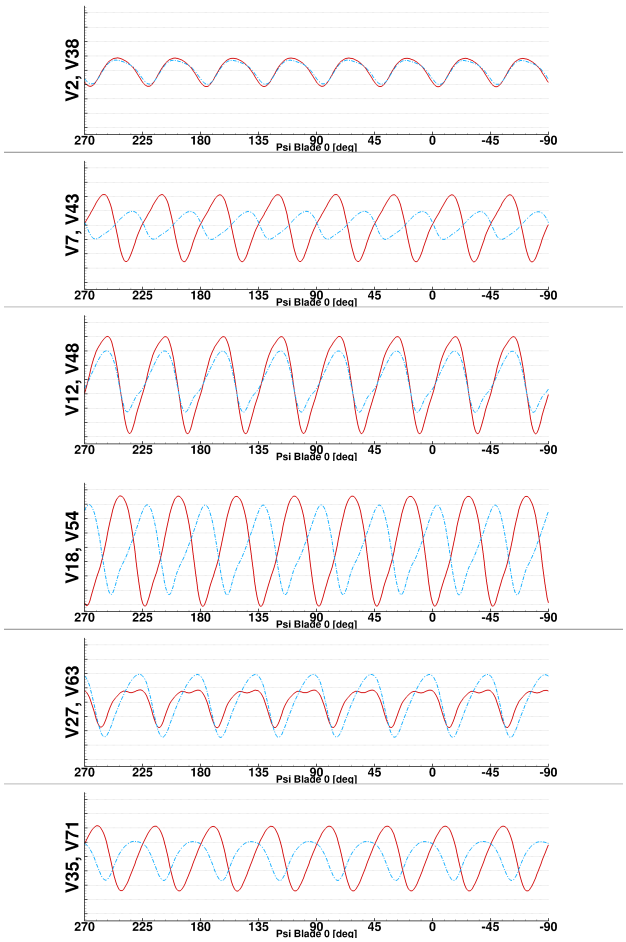
(c) $Z = 4c$ ($\psi_b = 270deg$). (d) $Z = 4c$ ($\psi_b = 90deg$).

Figure 9: Instantaneous acoustic pressure field, visualised in longitudinal planes.



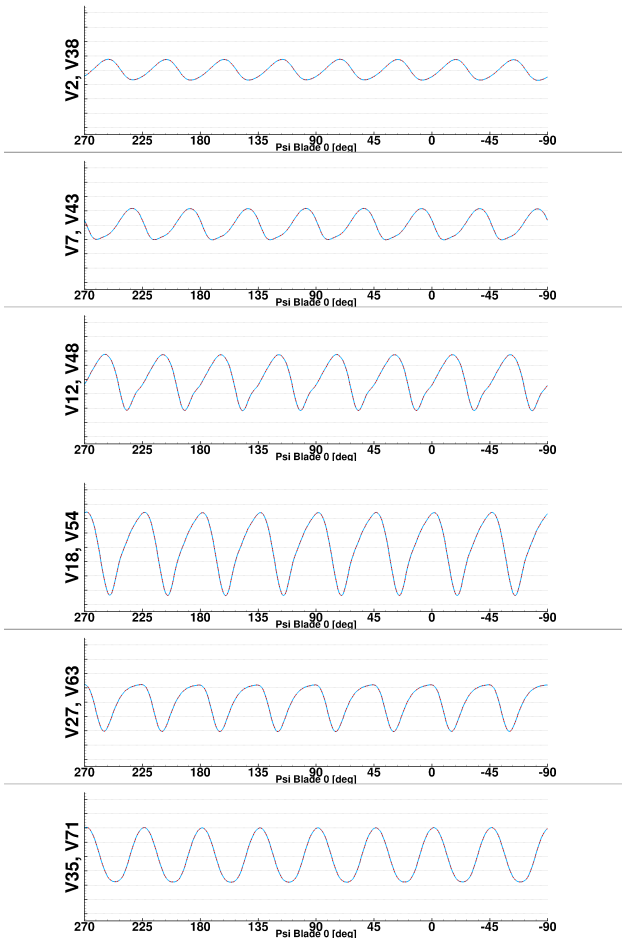
(a) Positions of the selected probes for the acoustic pressure signals analysis.

CO-ROTATING LAYOUT



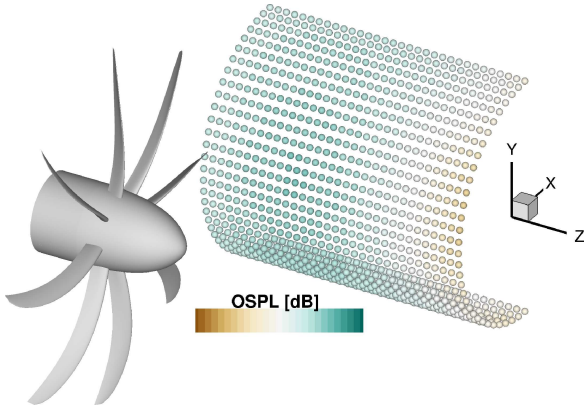
(b) Fifth propeller revolution.

COUNTER-ROTATING TOP-IN LAYOUT

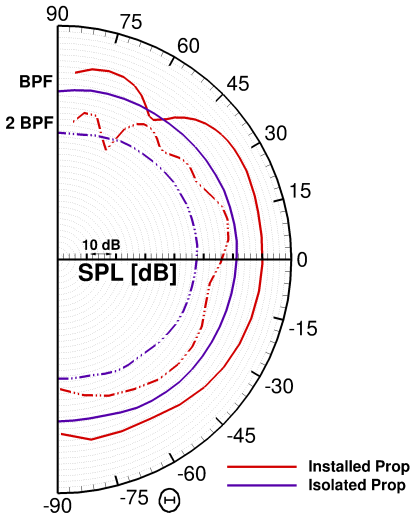


(c) Third propeller revolution.

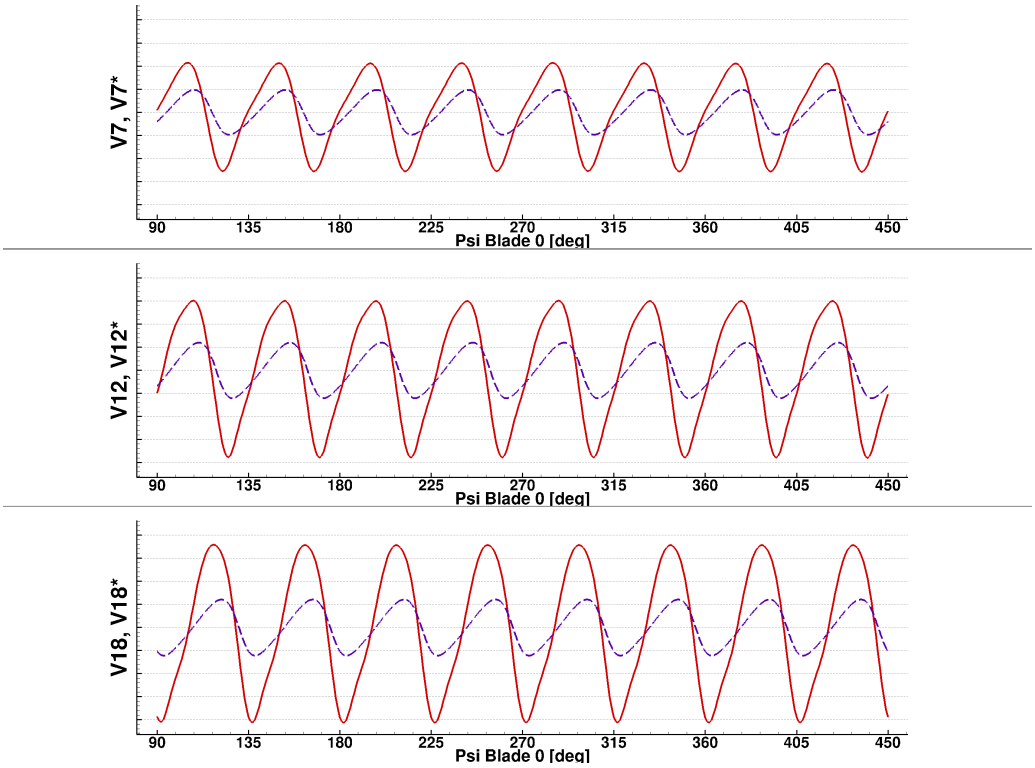
Figure 10: Unsteady pressure time history - URANS results over one revolution. Signals relative to the port side in light-blue and to the starboard side in red.



(a) OSPL visualisation on the idealised fuselage. Colour scale equal to that of Figure 6.



(b) SPL trend along the fuselage azimuth at the propeller plane.



(c) Unsteady pressure time history on the fuselage at the propeller plane - URANS results over one revolution. Refer to Figure 10(a) for the probe locations.

Figure 11: Comparison between installed and isolated acoustic estimates: starboard fuselage side with propeller rotating inboard up, i.e. co-rotating layout.

REFERENCES

[1] Pedro Argüelles, Manfred Bischoff, Philippe Busquin, BAC Droste, Sir Richard Evans, W Kröll, JL Lagardere, A Lina, J Lumsden, D Ranque, et al. European Aeronautics: a Vision for 2020 - Meeting Society's Needs and Winning Global Leadership. *Advisory Council for Aeronautics Research in Europe, Report*, 2001. URL http://www.acare4europe.org/sites/acare4europe.org/files/document/Vision%202020_0.pdf.

[2] The High Level Group on Aviation Research: M. Darecki, C. Edelstenne, T. Enders, E. Fernandez, P. Hartman, J.-P. Herteman, M. Kerkloh, I. King, P. Ky, M. Mathieu, G. Orsi, G. Schotman, C. Smith, and J.-D. Wörner. Flightpath 2050: Europe's vision for aviation. *Report of the High Level Group on Aviation Research, Publications Office of the European Union, Luxembourg*, 2011. URL http://ec.europa.eu/transport/sites/transport/files/modes/air/doc/flightpath2050.pdf.

[3] IMPACTA - IMproving the Propulsion Aerodynamics and aCoustics of Turboprop Aircraft. URL http://gtr.rcuk.ac.uk/project/506AE188-48A3-4C80-B96C-40E7120FFB75#.

[4] J.H. Dittmar and D.B. Stang. Cruise noise of the 2/9th scale model of the Large-scale Advanced Propfan (LAP) propeller, SR-7A. Technical Report NASA-TM-100175, E-3746, NAS 1.15:100175, NASA Lewis Research Center; Cleveland, OH, United States, September 1987. URL https://ntrs.nasa.gov/archive/nasa/casi.ntrs.nasa.gov/19870018965.pdf.

[5] RICHARD WOODWARD. Measured noise of a scale model high speed propeller at simulated takeoff/approach conditions. In *25th AIAA Aerospace Sciences Meeting*, page 526, 1987. doi: http://dx.doi.org/10.2514/6.1987-526. URL https://ntrs.nasa.gov/archive/nasa/casi.ntrs.nasa.gov/19870007155.pdf.

[6] R.P. Woodward and I.J. Loeffler. In-flight source noise of an advanced large-scale single-rotation propeller. *Journal of Aircraft*, 30(6):918–926, 1993. doi: http://dx.doi.org/10.2514/3.46435.

[7] R.P. Woodward and I.J. Loeffler. In-flight near-and far-field acoustic data measured on the Propfan Test Assessment (PTA) testbed and with an adjacent aircraft. Technical Report NASA-TM-103719, E-6402, NAS 1.15:103719, NASA Lewis Research Center; Cleveland, OH, United States, April 1993. URL https://ntrs.nasa.gov/archive/nasa/casi.ntrs.nasa.gov/19930017869.pdf.

[8] M. H. Dunn and F. Farassat. High-speed propeller noise prediction-a multidisciplinary approach. *AIAA journal*, 30(7):1716–1723, 1992. doi: http://dx.doi.org/10.2514/3.11128.

[9] P. Spence and P. Block. Analysis of the pta external noise data and comparison with predictions. In *13th Aeroacoustics Conference*, page 3935, 1990. doi: http://dx.doi.org/10.2514/6.1990-3935.

[10] M. H. Dunn and G. M. Tarkenton. Computational methods in the prediction of advanced subsonic and supersonic propeller induced noise: ASSPIN users' manual. Technical Report NASA-CR-4434, NAS 1.26:4434, NASA. Langley Research Center, Washington, United States, 1992. URL https://ntrs.nasa.gov/search.jsp?R=19920012215.

[11] F Farassat, SL Padula, and MH Dunn. Advanced turboprop noise prediction based on recent theoretical results. *Journal of Sound and Vibration*, 119(1):53–79, 1987. doi: https://doi.org/10.1016/0022-460X(87)90189-1.

[12] P. Spence. Development of a boundary layer noise propagation code and its application to advanced propellers. In *29th Aerospace Sciences Meeting*, page 593, 1991. doi: http://dx.doi.org/10.2514/6.1991-593.

[13] D.B. Hanson. Near-field frequency-domain theory for propeller noise. *AIAA journal*, 23(4):499–504, 1985. doi: http://dx.doi.org/10.2514/3.8943.

[14] E Envia. Prediction of noise field of a propfan at angle of attack. Technical Report NASA-CR-189047, E-6645, NAS 1.26:189047, NASA, United States, October 1991. URL https://ntrs.nasa.gov/archive/nasa/casi.ntrs.nasa.gov/19920004541.pdf.

[15] M. Nallasamy and F. Groenewg. Unsteady euler analysis of the flowfield of a propfan at an angle ofattack. *Journal of Propulsion and Power*, 8(1):136–143, 1992. doi: http://dx.doi.org/10.2514/3.23453.

[16] A. Dumas and C. Castan. Aerodynamic Integration of High Speed Propeller on Aircraft Recent Investigations in European Wind Tunnels. *21st ICAS Congress*, (ICAS-98-5,10,3), 1998.

[17] M Amato, F Boyle, J Eaton, and P Gardarein. Euler/navier-stokes simulation for propulsionairframe integration of advanced propeller-driven aircraft in the european research programs gemini/apian. *ICAS 98-5.10.2*, 10, 1998. URL http://www.icas.org/ICAS_ARCHIVE/ICAS1998/PAPERS/5102.PDF.

[18] J.M. Bousquet and P. Gardarein. Improvements on computations of high speed propeller unsteady aerodynamics. *Aerospace science and technology*, 7(6):465–472, 2003. doi: https://doi.org/10.1016/S1270-9638(03)00046-4.

[19] J. Frota and E. Maury. Analysis of APIAN high speed isolated test results - Acoustics and Aerodynamics. *Air and Space Europe*, 3(3-4):87–92, 2001. doi: https://doi.org/10.1016/S1290-0958(01)90064-4.

[20] C. Polacsek, P. Spiegel, F. Boyle, J. Eaton, H. Brouwer, and R. Nijboer. Noise computation of high-speed propeller-driven aircraft. In *6th Aeroacoustics Conference and Exhibit*, page 2086, 2000. doi: http://dx.doi.org/10.2514/6.2000-2086.

[21] I. Samuelsson. Low speed wind tunnel investigation of propeller slipstream aerodynamic effects on different nacelle/wing combinations. In *ICAS, Congress, 16 th, Jerusalem, Israel*, pages 1749–1765, 1988. URL `http://www.icas.org/ICAS_ARCHIVE/ICAS1988/ICAS-88-4.11.1.pdf`.

[22] I. Samuelsson. Experimental investigation of low speed model propeller slipstream aerodynamic characteristics including flow field surveys and nacelle/wing static pressure measurements. In *ICAS, Congress, 17 th, Stockholm, Sweden*, pages 71–84, 1990. URL `http://www.icas.org/ICAS_ARCHIVE/ICAS1990/ICAS-90-3.1.3.pdf`.

[23] P. Lotsted. Propeller slip-stream model in subsonic linearized potential flow. *Journal of Aircraft*, 29(6):1098–1105, 1992. doi: http://dx.doi.org/10.2514/3.56865.

[24] P. Lotsted. A propeller slipstream model in subsonic linearized potential flow. In *ICAS, Congress, 17 th, Stockholm, Sweden*, pages 733–744, 1990. URL `http://www.icas.org/ICAS_ARCHIVE/ICAS1990/ICAS-90-5.4.4.pdf`.

[25] A. Stuermer. Unsteady euler and navier-stokes simulations of propellers with the unstructured dlr tau-code. In *New Results in Numerical and Experimental Fluid Mechanics V*, pages 144–151. Springer, 2006. doi: DOI:10.1007/978-3-540-33287-9_18.

[26] S. Leth, F. Samuelsson, and S. Meijer. Propeller Noise Generation and its Reduction on the Saab 2000 High-Speed Turboprop. (AIAA-98-2283):457–463, 1998.

[27] G.N. Barakos, R. Steijl, K. Badcock, and A. Brocklehurst. Development of CFD Capability for Full Helicopter Engineering Analysis. *31th European Rotorcraft Forum, Florence, Italy, Sept*, 2005.

[28] R. Steijl, G. Barakos, and K. Badcock. A Framework for CFD Analysis of Helicopter Rotors in Hover and Forward Flight. *International Journal for Numerical Methods in Fluids*, 51(8):819–847, 2006. doi: 10.1002/fld.1086.

[29] J. Boussinesq. *Théorie de l'Écoulement Tourbillonant et Tumultueux des Liquides dans des Lits Rectilignes à Grande Section, Tome I-II*. Gaulthier-Villars, Paris, France, first edition, 1897.

[30] A.K. Hellsten. New advanced kw turbulence model for high-lift aerodynamics. *AIAA journal*, 43(9):1857–1869, 2005. doi: 10.2514/1.13754.

[31] F. R. Menter. Two-Equation Eddy-Viscosity Turbulence Models for Engineering Applications. *AIAA Journal*, 32(8):1598–1605, August 1994. doi: http://dx.doi.org/10.2514/3.12149.

[32] S. Osher and S. Chakravarthy. Upwind Schemes and Boundary Conditions with Applications to Euler Equations in General Geometries. *Journal of Computational Physics*, 50(3):447–481, 1983. doi: 10.1016/0021-9991(83)90106-7.

[33] B. van Leer. Flux-vector Splitting for the Euler Equations. In *Upwind and High-Resolution Schemes*, volume 1, pages 80–89. Springer Berlin Heidelberg, 1997. ISBN 978-3-642-64452-8. doi: 10.1007/978-3-642-60543-7_5.

[34] G.D. van Albada, B. van Leer, and W.W. Roberts Jr. A Comparative Study of Computational Methods in Cosmic Gas Dynamics. In *Upwind and High-Resolution Schemes*, volume 2, pages 95–103. Springer Berlin Heidelberg, 1997. ISBN 978-3-642-64452-8. doi: 10.1007/978-3-642-60543-7_6.

[35] O. Axelsson. *Iterative Solution Methods*. Cambridge University Press, Cambridge, MA, edition, 1994. ISBN 0-521-44524-8.

[36] S. J. Lawson, M. Woodgate, R. Steijl, and G. N. Barakos. High Performance Computing for Challenging Problems in Computational Fluid Dynamics. *Progress in Aerospace Sciences*, 52:19–29, July 2012. doi: http://dx.doi.org/10.1016/j.paerosci.2012.03.004.

[37] N. Scrase and M. Maina. The evaluation of propeller aero-acoustic design methods by means of scaled-model testing employing pressure tapped blades and spinner. In *ICAS PROCEEDINGS*, volume 19, pages 183–183. AMERICAN INST OF AERONAUTICS AND ASTRONAUTICS, 1994.

[38] G.N. Barakos and C.S. Johnson. Acoustic comparison of propellers. *International Journal of Aeroacoustics*, 15(6-7):575–594, 2016. doi: https://doi.org/10.1177/1475472X16659214.

[39] A. Gomariz-Sancha, M. Maina, and A. J. Peace. Analysis of Propeller-Airframe Interaction Effects through a Combined Numerical Simulation and Wind-Tunnel Testing Approach. *AIAA SciTech, 53rd AIAA Aerospace Sciences Meeting, Kissimmee, Florida*, page 1026, 2015. doi: doi:10.2514/6.2015-1026.

[40] R. Steijl and G. Barakos. Sliding Mesh Algorithm for CFD Analysis of Helicopter Rotor˘Fuselage Aerodynamics. *International Journal for Numerical Methods in Fluids*, 58:527–549, 2008. doi: 10.1002/fld.1757.

[41] G. Chirico and G.N. Barakos. Computational aeroacoustic analysis of propeller configurations. In *Applied Aerodynamics Research Conference Proceedings*. Royal Aeronautical Society, 2016.

[42] ANSYS ICEM CFD. URL `http://www.ansys.com/Products/Other+Products/ANSYS+ICEM+CFD/`.

[43] M. Jarwowsky, M.A. Woodgate, G. Barakos, and J. Rokicki. Towards Consistent Hybrid Overset Mesh Methods for Rotorcraft CFD. *International Journal for Numerical Methods in Fluids*, 74:543–576, 2014.

[44] Aircraft Noise Committee. Estimation of the Maximum Discrete Frequency Noise from Isolated Rotors and Propellers. Technical Report Aerounautical Series 76020, ESDU, March 2011.

[45] L. Gutin. On the Sound of a Rotating Propeller. Technical Report TM-1195, NACA-National Advisory Committee for Aeronautics., Langley Aeronautical Lab.; Langley Field, VA, United States, October 1948. URL `https://ntrs.nasa.gov/search.jsp?R=20030068996`.

[46] L.L.M. Veldhuis. Review of Propeller-Wing Aerodynamic Interference. *ICAS - 24th International Congress of the Aeronautical Sciences*, 2004.

[47] J.F. Johnston, R.E. Donham, and W.A. Guinn. Propeller signatures and their use. *Journal of Aircraft*, 18(11):934–942, 1981. doi: http://dx.doi.org/10.2514/3.57583.

[48] B. Magliozzi. Synchrophasing for cabin noise reduction of propeller-driven airplanes. In *8th Aeroacoustics Conference*, page 717, 1983. doi: http://dx.doi.org/10.2514/6.1983-717.

[49] C.R. Fuller. Noise control characteristics of synchrophasing. i-analytical investigation. *AIAA journal*, 24(7):1063–1068, 1986. doi: http://dx.doi.org/10.2514/3.9392.

[50] J.D. Jones and C.R. Fuller. Noise control characteristics of synchrophasing. ii-experimental investigation. *AIAA journal*, 24(8): 1271–1276, 1986. doi: http://dx.doi.org/10.2514/3.9431.

[51] D.M. Blunt and B. Rebbechi. Propeller synchrophase angle optimisation study. In *13th AIAA/CEAS Aeroacoustics Conference (28th AIAA Aeroacoustics Conference)*, page 3584, 2007. doi: http://dx.doi.org/10.2514/6.2007-3584.

[52] F. R. Menter and Y. Egorov. A Scale Adaptive Simulation Model using Two-Equation Models. *43rd AIAA Aerospace Sciences Meeting and Exhibit*, 2005. doi: http://dx.doi.org/10.2514/6.2005-1095.

[53] M. Strelets. Detached Eddy Simulation of Massively Separated Flows. In *AIAA 39th Aerospace Sciences Meeting and Exhibit, Reno, NV*, January 8–11 2001. AIAA-2001-0879.

[54] Michael L Shur, Philippe R Spalart, and Michael K Strelets. Jet noise computation based on enhanced des formulations accelerating the rans-to-les transition in free shear layers. *International Journal of Aeroacoustics*, 15(6-7):595–613, 2016. doi: https://doi.org/10.1177/1475472X16659388.

[55] A. Jimenez Garcia and G. N. Barakos. Implementation of high-order methods in the hmb cfd solver. In *73rd AHS International's Annual Forum and Technology Display*, 2017.

[56] Dowty Aerospace Propellers. URL `http://dowty.com`.